Article

Not peer-reviewed version

Exploration of Structural, Thermodynamic, Magnetic and Mechanical Properties of Martensite Fe_3Pt Alloys: A Density Functional Theory Study

N. L. Lethole * and E. H. Onah

Posted Date: 29 October 2025

doi: 10.20944/preprints202510.2084.v1

Keywords: martensite Fe_3Pt; thermodynamic stability; magnetic moments; mechanical stability; spin asymmetry

Article

Exploration of Structural, Thermodynamic, Magnetic and Mechanical Properties of Martensite Fe_3Pt Alloys: A Density Functional Theory Study

N. L. Lethole* and E. H. Onah

Department of Computational Sciences, University of Fort Hare, Private Bag X1314, Alice, 5700, RSA

* Correspondence: nlethole@ufh.ac.za

Abstract

The current study explored the martensite structures of Fe_3Pt alloys, specifically $Cmmm$-Fe_3Pt, $P63/mmc$ -Fe_3Pt, $P4/mmm$ -Fe_3Pt, and $R\bar{3}m$ -Fe_3Pt, aiming to provide a comprehensive understanding of the mechanisms that govern their physical and chemical properties. We have focused on their structural, thermodynamical, magnetic, electronic, and mechanical characteristics, utilizing the Density Functional Theory (DFT) technique. Our study revealed that in addition to the previously reported austenitic cubic $Pm\bar{3}m$-Fe_3Pt and martensite tetragonal $I4/mmm$-Fe_3Pt with $L1_2$ structure, there exist additional Fe_3Pt phases that exhibit excellent structural, thermodynamic, magnetic and mechanical properties. The calculated enthalpies of formation were found to be negative and less than -0.39 eV in all the structures considered, indicating thermodynamic stability and formation under experimental synthetic conditions. Moreover, the computed magnetic moments are in the range 2.94 to 3.04 μ_B, which is relatively comparable to 3.24 μ_B of the widely reported $Pm\bar{3}m$-Fe_3Pt alloy. The analysis of the electronic structure also revealed strong magnetism due to the presence of asymmetry in the spin up and down states of the density of states (DOS) plots. To determine the mechanical response of Fe_3Pt structures under loading conditions, we computed the independent elastic constants, macroscopic properties and stress-strain relationship under hydrostatic stress. All four phases, but the hypothetical $P63/mmc$ -Fe_3Pt showed excellent mechanical stability at ambient conditions and exceptional hardness and resistance to compression in the elastic region 0% ≤ strain ≤ 10%. This evidence is provided by satisfying the Born necessary stability conditions, large bulk modulus and a strong linear relationship fit (R^2) of greater than 0.94.

Keywords: martensite Fe_3Pt; thermodynamic stability; magnetic moments; mechanical stability; spin asymmetry

1. Introduction

The exploration of bimetallic Fe-Pt alloys has long garnered significant attention due to their intriguing properties and promising applications in various fields such as ultra-high density data storage, spintronics, catalysis, and nanotechnology [1, 2, 3, 4]. As indicated by their binary stability phase diagram [5], there have been three well-known and widely reported structures of Fe-Pt alloys which are chemically ordered. These include the tetragonal $L1_0$ $P4/mmm$-FePt phase which exhibits ferromagnetic ordering, and the face-centered cubic (FCC) phases $FePt_3$ and Fe_3Pt, both crystallizing in the $Pm\bar{3}m$ space group with $L1_2$-type crystal symmetry. The latter two phases support both antiferromagnetic and ferromagnetic magnetic ordering [6]. These alloys have been previously investigated both experimentally and computationally and have been found to exhibit excellent thermodynamic, vibrational and mechanical stability. Moreover, they possess desirable magnetic properties due to large magnetic moments, large uniaxial magnetocrystalline anisotropy (MCA) energies originating from spin-orbit interactions and asymmetry of spin up and down in the electronic density of states [7, 8, 9]. Variations in crystallization and chemical composition

 doi:10.20944/preprints202510.2084.v1

significantly influence their magnetic behavior, electronic structure, and lattice dynamics. For instance, although both Fe and Pt contribute to the magnetic moments, Fe contributes approximately eight times more than Pt, thereby making the magnetic behavior predominantly dependent on the Fe content [10]. The $P4/mmm$-FePt phase crystallizes at temperatures below 1570 K in equiatomic Fe:Pt concentration, while the FCC structures crystallize around 25 % and 75 % Fe contents at temperatures below 1120 K and 1620 K, respectively [11]. The tetragonal $L1_0$ FePt shows one of the highest MCA energy ranging from $6 \times 10^6 J/m^3$ to $9 \times 10^6 J/m^3$ along the magnetically easy c axis [001], making it a promising candidate to overcome superparamagnetic limit, which is the loss data due to thermally activated fluctuations of magnetization [12, 13]. It consists of alternating stacked atomic layers of Fe and Pt atoms along [100] direction similar to the AuCu structure, leading to a tetragonal distortion along the c-axis. As per the previous communication, the cubic Fe_3Pt and $FePt_3$ alloys exhibit the highest MCA energies of $1.1 \times 10^6 J/m^3$ (0.375 meV) and $1.5 \times 10^5 J/m^3$ (0.055 meV) along the [100] easy axis [12]. In the Fe-rich Fe_3Pt alloy, Fe atoms occupy the corner lattice positions, while Pt atoms are located at face-centered positions. Conversely, in the Pt-rich $FePt_3$ alloy, Pt atoms occupy the corner positions, and Fe atoms are situated at the face-centered positions.

In addition, the $L1_2$ face-centered cubic (austenitic) Fe_3Pt alloy is reported to exhibit strong magnetoelastic coupling and undergoes a thermoelastic martensitic transformation from the ordered $L1_2$ phase into low-temperature martensitic structures, which inherently depend on the degree of order of the $L1_2$ structure [14, 15]. One such martensite structure is the body-centered tetragonal (BCT) Fe_3Pt phase, which crystallizes in the $I4/mmm$ space group [16, 17]. The equilibrium cell parameters of the $I4/mmm$ bulk structure as produced by X-ray diffraction are $a = 5.73$ Å and $c = 6.34$ Å [18]. It was found that the spin up Fe d states in the density of states (DOS) in this martensite structure are situated below the Fermi level, while the spin down states overlaps above the Fermi, indicating a pronounced spin asymmetry. Consequently, this spin polarization results in relatively large magnetic moments of 2.61 μ_B and 2.82 μ_B for Fe1 and Fe2 atoms, respectively. Moreover, Pt atoms were also found to exhibit a finite magnetic moment of 0.45 μ_B, suggesting a degree of spin polarization induced by hybridization with neighboring Fe atoms [16]. Our previous communication further reported magnetic moments of 2.744 μ_B for Fe and 0.45 μ_B Pt along with the MCA energy of 1.364 meV along the [001] easy axis [12], which are higher than those of the austenitic Fe_3Pt.

The structural models of other Fe_3Pt martensite phases have long been proposed, however, their properties remain unstudied [19]. According to the Materials Explorer within the Materials Project database [20, 21], three additional martensitic phases of Fe_3Pt are predicted to exist whose structural, thermodynamic, magnetic and mechanical properties are not yet fully explored. These correspond to the $P4/mmm$, $Cmmm$, and $R3m$ space groups as shown in Figure 1. The $Cmmm$–Fe_3Pt phase crystallizes at approximately 55 K in an orthorhombic lattice characterized by primitive lattice parameters $(a = 3.732$ Å$, b = 3.714$ Å$, \mathrm{c} = 3.750$ Å$)$ as determined by XRD. The structure comprises two crystallographically distinct Fe sites. This orthorhombic structure is an intermediate phase, appearing between face-centered tetragonal (FCT1) ($c/a < 1$) and FCT2 ($c/a > 1$) [15]. The system considered in this current work is a conventional c-centered (centering doubles the number of lattice points along one direction) orthorhombic Fe_3Pt which is equivalent, but twice the volume and number of atoms (eight) as the primitive (four atoms) reported in literature. In the first site, Fe atoms adopt a two-coordinate geometry, bonded to two Fe and two Pt atoms, whereas the second Fe site exhibits eightfold coordination with neighboring Fe atoms. The Pt atoms display a four-coordinate geometry, each bonded to four Fe atoms, completing the orthorhombic network. The $P4/mmm$–Fe_3Pt phase exhibits a USi_2-type structure and crystallizes in a body centered tetragonal (BCT) lattice. This phase forms through a thermoelastic transformation. During the formation, the tetragonality ratio c/a shifts from 1 to 0.79 at the transformation temperature, signifying a discontinuous lattice distortion characteristic of a first-order martensitic transformation [15, 17]. The structure contains two inequivalent Fe sites. Each Fe atom is coordinated by eight Fe and four Pt atoms, forming distorted $FeFe_8Pt_4$ cuboctahedra. These polyhedra interconnect through corner-, edge-, and face-sharing with neighboring $FeFe_8Pt_4$ and $PtFe_{12}$ units, forming a highly integrated three-dimensional framework.

 doi:10.20944/preprints202510.2084.v1

The Pt atoms are twelvefold coordinated by Fe atoms, generating $PtFe_{12}$ cuboctahedra that are similarly interconnected through shared corners, edges, and faces with surrounding $FeFe_8Pt_4$ polyhedra. The $R\bar{3}m$–Fe_3Pt phase crystallizes in a rhombohedral centered hexagonal or trigonal lattice. Each Fe atom is surrounded by nine Fe and three Pt atoms, forming distorted $FeFe_9Pt_3$ cuboctahedra that share corners, edges, and faces with adjacent $FeFe_9Pt_3$ and $PtFe_6Pt_6$ polyhedra. The Pt atoms are coordinated by six Fe and six Pt atoms, creating $PtFe_6Pt_6$ cuboctahedra that link through corner-, edge-, and face-sharing, producing a robust trigonal framework. Lastly, the $P63/mmc$-Mn_3Ir structure served as a prototype for Fe_3Pt, since Fe and Mn as well as Pt and Ir are chemically analogous neighboring transition metals with comparable atomic radii and electronic configurations. Such substitution preserves the symmetry and coordination environment, enabling reliable DFT modeling of synthetical Fe–Pt system within the same crystallographic framework. This is beta Cu_3Ti and Mn_3Ga type structure which crystallizes in the hexagonal lattice with eight atoms in a primitive cell [22, 23]. Fe is bonded to four equivalent Pt atoms to form a mixture of distorted corner, edge, and face-sharing $FePt_4$ cuboctahedra. Pt is bonded to twelve equivalent Fe atoms to form a mixture of corner and face-sharing $PtFe_{12}$ cuboctahedra.

The magnetic, thermodynamic and mechanical properties of these four martensite phases are yet to be systematically explored either experimentally or theoretically, which limits a comprehensive understanding of the structure–property relationships and the potential functional applicability in advanced magnetic and electronic technologies. Experimental exploration of these alloys may be challenging due to the complexities associated with detecting such phases arising from dynamical effects on diffraction reflections [16]. However, the development of density functional theory (DFT)-based first-principles methods enables theoretical exploration and optimization of $L1_2$ bimetallic alloys by accurately calculating the interatomic forces acting on the nuclei [24, 25, 26]. The current study focuses on the structural, thermodynamic, magnetic, electronic and mechanical properties of the four martensite Fe_3Pt bimetallic alloys at 0K to assess their stability and deduce their suitability as magnetic materials. We have employed the density functional theory (DFT) quantum mechanical method embedded in the CASTEP code to perform first-principles quantum mechanical calculations on Fe_3Pt alloys. Our computational findings revealed that three martensite Fe_3Pt alloys exhibit excellent thermodynamic and mechanical stability and magnetic moments comparable to those of the extensively studied Fe-Pt alloys.

 doi:10.20944/preprints202510.2084.v1

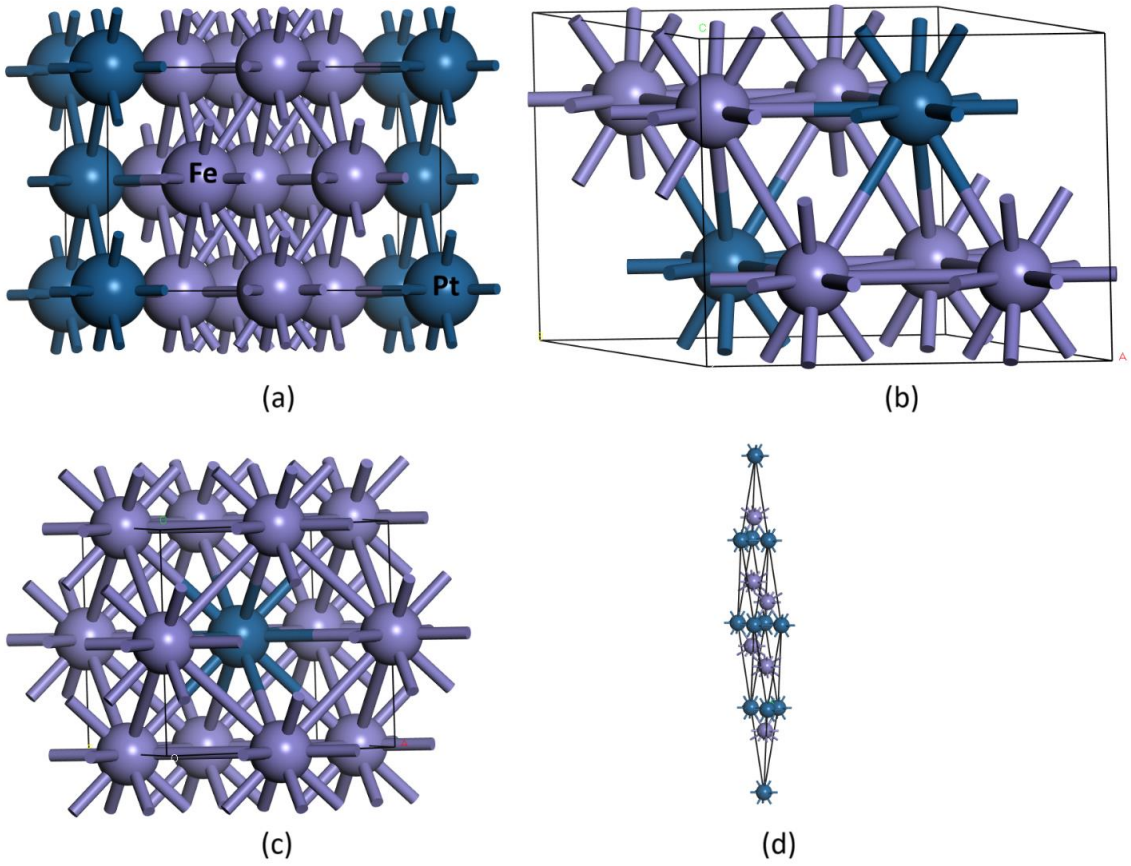

Figure 1. Schematic representation of atomic arrangements in (a) $Cmmm$ (b) $P63/mmc$ (c) P4/mmm and (d) R3m Fe_3Pt alloys.

2. Computational Approach

The present study utilized the Cambridge Serial Total Energy Package (CASTEP) [27] which employs the plane-wave density functional theory (DFT) plane-wave pseudopotential method to perform first-principles calculations on Fe_3Pt alloys. The Generalized Gradient Approximation (GGA) and Perdew-Burke-Ernzerhof (PBE) exchange-correlation functional were preferred since they account for inhomogeneities in the electron distribution [28, 29]. To determine the minimum optimal plane-wave cut-off energies that converge the total energy, single-point energy calculations were performed for all the systems at several increasing cut-off values without relaxing the atomic positions and cell parameters. This was done until the total energy between successive steps was below 1 meV. The cut-off energies 400 eV, 300 eV, 400 eV and 300 eV were respectively found sufficiently to converge the total energies of $Cmmm$, $P63/mmc$, $P4/mmm$ and $R\bar{3}m$ systems. Moreover, the customized Monkhorst-Pack [30] k-points grid size of 9x7x4, 4x4x6, 5x5x6 and 8x8x1 for self-consistent field (SCF) calculations were applied for Brillouin zone sampling. Before subsequent calculations of electronic structure and elastic properties, full geometry optimization was performed to obtain the arrangement of atoms and cell parameters corresponding to the minimum total energy and zero net forces on atoms, i.e. the ground-state structures. Both cell volume and shape were allowed to change until the final energy between two iterations was less than 5.7 meV. To allow separation of majority and minority spin projections, the spin density was treated by the collinear spin polarization using formal spin as initial. The low-memory Brayden-Fletcher-Goldfarb-Shanno (LBFGS) algorithm [31] that scales linearly in memory and performs better for large systems was preferred for cell optimization over the normal BFGS [32] that scales as a square of the system size for cell. Furthermore, the LBFGS algorithm employs a general sparse preconditioner that enhances the efficiency of geometry optimization, achieving up to a twofold speed increase for small systems

 doi:10.20944/preprints202510.2084.v1

and up to tenfold for large systems [33]. Subsequent computation of density of states and elastic constants were done using the equilibrium structures. Calculation of the elastic properties was performed using the Elastic Constants task with a maximum strain amplitude of 0.003, which is adequately low for the material to stay in the linear elasticity. The calculation of electronic band structure and density of states was done with and band energy tolerance of 10^{-5} eV.

3. Results and Discussion

3.1. Structural Properties

The equilibrium cell parameters, densities and enthalpies of formation of the four martensite Fe_3Pt structure as shown in Table 1 were obtained by performing full geometry optimization. The experimental volume for the orthorhombic $Cmmm$-Fe_3Pt and lattice parameters of the previously reported austenitic $Pm\bar{3}m$ -Fe_3Pt are given in parenthesis to validate DFT calculations against existing experimental data. The calculated lattice parameters of $Pm\bar{3}m$ -Fe_3Pt are more than 99 % in agreement with experimental data [34] and previous calculations [8], while the optimized volume of $Cmmm$-Fe_3Pt in 96 % in agreement with the XRD results [15]. These agreements indicate that the employed approach correctly predicts the ground state properties of Fe_3Pt alloys. The conventional hexagonal $P63/mmc$-Fe_3Pt structure shows the largest unit cell volume and smallest density corresponding to weaker interatomic interactions. The enthalpies of formation (ΔH_f) were computed according to equation 1,

$$\Delta H_f = E_{Fe_3Pt} - \sum_i n_i E_i^{element} \quad (1)$$

where E_{Fe_3Pt} is the total ground state energy of Fe_3Pt formula unit and $E_i^{element}$ the elemental energies of Fe and Pt atoms. Negative enthalpies of formation indicate the release of energy when forming a compound (exothermic reaction) and thus thermodynamic stability of the compounds in relation to its constituent elements, i.e. $E_{compound} < E_{elements}$. Our DFT calculations predict that all the four martensite Fe_3Pt alloys are thermodynamically stable due to negative enthalpies of formation. Expectedly, the enthalpy of formation values of austenitic $Pm\bar{3}m$ and martensite $Cmmm$, $P63/mmc$, $P4/mmm$ and $R\bar{3}m$ are similar since they have the same stoichiometry and elemental reference state.

Table 1. Calculated equilibrium cell parameters, densities and enthalpies of formation and density of Fe_3Pt alloys.

Parameter	$Pm\bar{3}m$	$Cmmm$	$P63/mmc$	$P4/mmm$	$R\bar{3}m$
a (Å)	3.756 (3.73) [34]	4.089	5.262	3.827	8.550
b (Å)	-	4.092			
c (Å)		6.197	4.685	3.593	
V (Å^3)	53.000	103.694	112.34	52.620	54.330
$\Delta H_f(eV/atom)$	-0.391	-0.391	-0.391	-0.391	-0.391
$\rho(g/cm^3)$	11.361	11.614	10.720	11.440	11.082

3.2. Magnetic Properties

Table 2 presents the calculated spin polarized magnetic moments and charge distribution characteristics of the four considered Fe_3Pt crystal structures derived from Mulliken atomic population analysis. The magnetic moments are calculated as the difference between spin up and spin down ($\uparrow - \downarrow$) charge densities. Moreover, the average of Fe1 and Fe2 were taken when quantifying the total spin moment per formula unit. The calculated total moments for $Cmmm$, $P63/mmc$, $P4/mmm$ and $R\bar{3}m$ are 3.01 μ_B, 3.04 μ_B, 2.94 μ_B and 2.97 μ_B, respectively. These values are comparable with those reported for other Fe-Pt alloys and bimetallic systems of similar composition [10, 35, 36]. For all space groups, the Fe atoms exhibit substantial local magnetic

 doi:10.20944/preprints202510.2084.v1

moments compared to Pt, indicative of strong ferromagnetic ordering within the Fe sublattice and large spin–orbit effects from Pt. Moreover, in all the structures, the spin up (↑) for both Fe1 and Fe2 are more densely than the spin down (↓) revealing pronounced spin asymmetry in the electronic density of states and confirming strong magnetic polarization within the system.

Our DFT calculations reveal that the orthorhombic $Cmmm$ space group possesses the largest Fe1 magnetic moment (2.98 μ_B), followed by the hexagonal $P63/mmm$ (2.92 μ_B), while the trigonal $R\bar{3}m$ and tetragonal $P4/mmm$ display relatively decreased moment values of 2.87 μ_B and 2.83 μ_B, respectively. This may be attributed to the increase of restrictions on independent lattice parameters and angles, i.e. symmetry from orthorhombic to tetragonal, which slightly decreases the exchange splitting, consistent with increased Fe–Pt orbital hybridization. The smaller variation in Fe2 moments indicates comparable local environments across the structures, except for the $P6_3/mmc$ phase, where Fe occupies only one unique crystallographic site due to higher symmetry. The Pt atoms exhibit relatively small induced magnetic moments, ranging from 0.12 μ_B to 0.30 μ_B, arising from Fe–Pt hybridisation and spin polarization of Pt 5d orbitals. $Cmmm$-Fe_3Pt shows the largest Pt moment (0.30 μ_B), whereas the $P63/mmm$ phase displays the smallest (0.12 μ_B).

Table 2. Calculated magnetic moments, Hirshfield spins and charges Fe_3Pt alloys.

Magnetic Moments (μ_B)				
	$Cmmm$	$P63/mmc$	$P4mmm$	$R\bar{3}m$
$Fe_1\uparrow$	5.35	5.33	5.29	5.34
$Fe_1\downarrow$	2.38	2.41	2.47	2.46
$\boldsymbol{Fe_1\uparrow - Fe_1\downarrow\ (\mu_B)}$	**2.98**	**2.92**	**2.83**	**2.87**
$Fe_2\uparrow$	5.18	-	5.26	5.29
$Fe_2\downarrow$	2.74	-	2.50	2.64
$\boldsymbol{Fe_2\uparrow - Fe_2\downarrow\ (\mu_B)}$	**2.43**	**-**	**2.75**	**2.65**
$Pt\uparrow$	16.46	16.45	16.43	16.34
$Pt\downarrow$	16.16	16.34	16.29	16.13
$\boldsymbol{Pt\uparrow - Pt\downarrow\ (\mu_B)}$	**0.30**	**0.12**	**0.15**	**0.21**
Total ($\mu_B/f.u.$)	**3.01**	**3.04**	**2.94**	**2.97**
Hirshfeld Analysis (μ_B)				
Fe_1	2.83	2.81	2.72	2.82
Fe_2	2.45	-	2.68	2.61
Pt	0.57	0.45	0.44	0.35
Charge (e)				
Fe_1	0.27	0.26	0.24	0.20
Fe_2	0.08	-	0.24	0.07
Pt	-0.62	-0.79	-0.72	-0.46

The Hirshfeld partitioning of electron density into atomic contributions further confirms the dominance of Fe atoms in the overall magnetic behavior. The Fe1 moments range from 2.72 μ_B to 2.83 μ_B, while Fe2 moments vary between 2.45 μ_B to 2.68 μ_B. In contrast, Pt contributes only 0.35-0.57 μ_B, consistent with the induced magnetization mechanism. The $Cmmm$ structure again exhibits the highest overall Fe magnetization, while the $P4/mmm$ phase shows a marginally reduced value, reflecting differences in local coordination and exchange interactions.

Hirshfeld charge analysis indicates notable charge redistribution between Fe and Pt atoms. Fe atoms possess positive charges (+0.07 to +0.27 e), signifying electron donation, while Pt atoms carry negative charges (−0.46 to −0.79 e), confirming their role as electron acceptors. The $P63/mmm$ phase shows the highest charge transfer (-0.79 e), suggesting stronger Fe–Pt bonding and more effective hybridization.

 doi:10.20944/preprints202510.2084.v1

3.3. Electronic Structure

Figure 2 presents the electronic total and orbital-projected spin polarized density of states (DOS) for the martensitic Fe_3Pt, with the Fermi level set as the origin of the energy scale. As anticipated, all the investigated Fe_3Pt alloys display metallic behavior, as indicated by the finite density of states at the Fermi level arising from the overlap of valence and conduction bands, most prominently in the spin-down states. In all total DOS plots, the spin-up states are predominantly located below the Fermi level, whereas the spin-down states extend into the conduction band above the Fermi level, reflecting a pronounced spin asymmetry which indicates spin polarization and gives rise to substantial magnetic moments and strong ferromagnetic character consistent with previous experimental findings on Fe_3Pt thin films [37]. Notably, the $P63/mmc$ phase exhibits a further strong asymmetry (enhanced spin polarization) in the valence states between −4 eV and −2 eV, consistent with its highest calculated magnetic moment. There exist shallow pseudo-gaps near the Fermi level, indicating enhanced Fe-Pt hybridization and electronic stability for all phases.

The orbital-projected DOS shows a dominant contribution from Fe 3d states in the total plots, with minor contribution from the Pt 5d states hybridizing with Fe d-bands. Moreover, there exist strong spin asymmetry in Fe states and weaker in Pt. This strong exchange splitting reflects localized Fe moments stabilized by the low structural symmetry. Furthermore, the strong spin polarization arises from the Fe 3d orbitals, while Pt-5d orbitals show small but non-zero induced moments, contributing slightly to the total magnetization.

 doi:10.20944/preprints202510.2084.v1

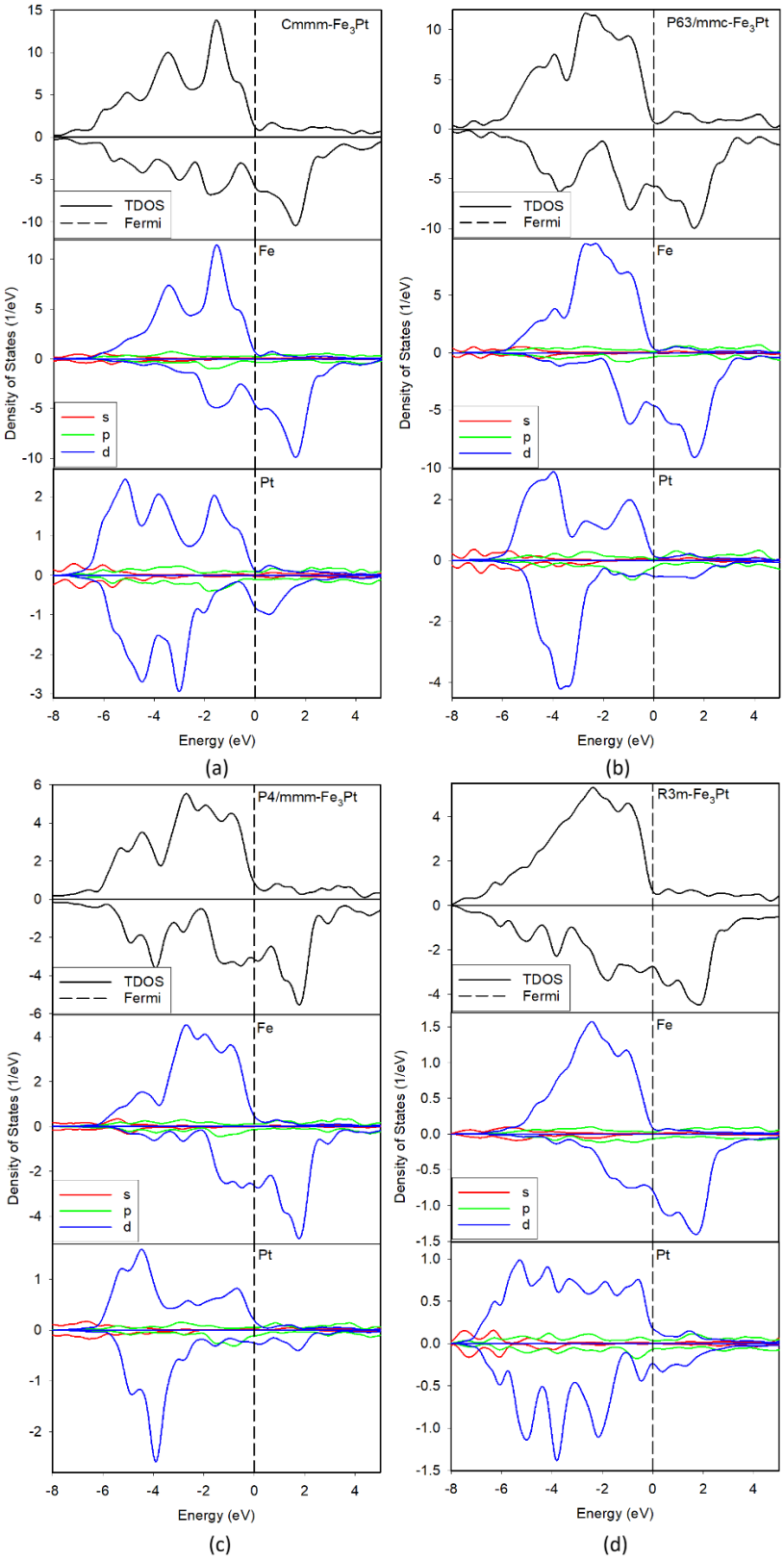

Figure 2. Total and partial density of states for $Cmmm$, $P63/mmc$, $P4/mmm$ and $R\bar{3}m$ Fe_3Pt alloys. The Fermi level is taken as the origin of the energy axis ($E_F = 0eV$).

The electronic properties of these systems were further analyzed using the band structure along high symmetry direction in the Brillouin zone as presented in Figure 3. All four structures exhibit metallic characteristics, as evidenced by the continuous overlap of energy bands at the Fermi level and the finite DOS at E_F and transitioning of electron wave highest to lowest energy levels through

 doi:10.20944/preprints202510.2084.v1

the Brillouin zone [38]. Moreover, there exists a clear spin splitting: red and blue bands diverge near the Fermi level. Interestingly, the $R\bar{3}m$ phase shows almost similar spin up (red) and spin down (blue) bands, indicating nearly degenerate spins.

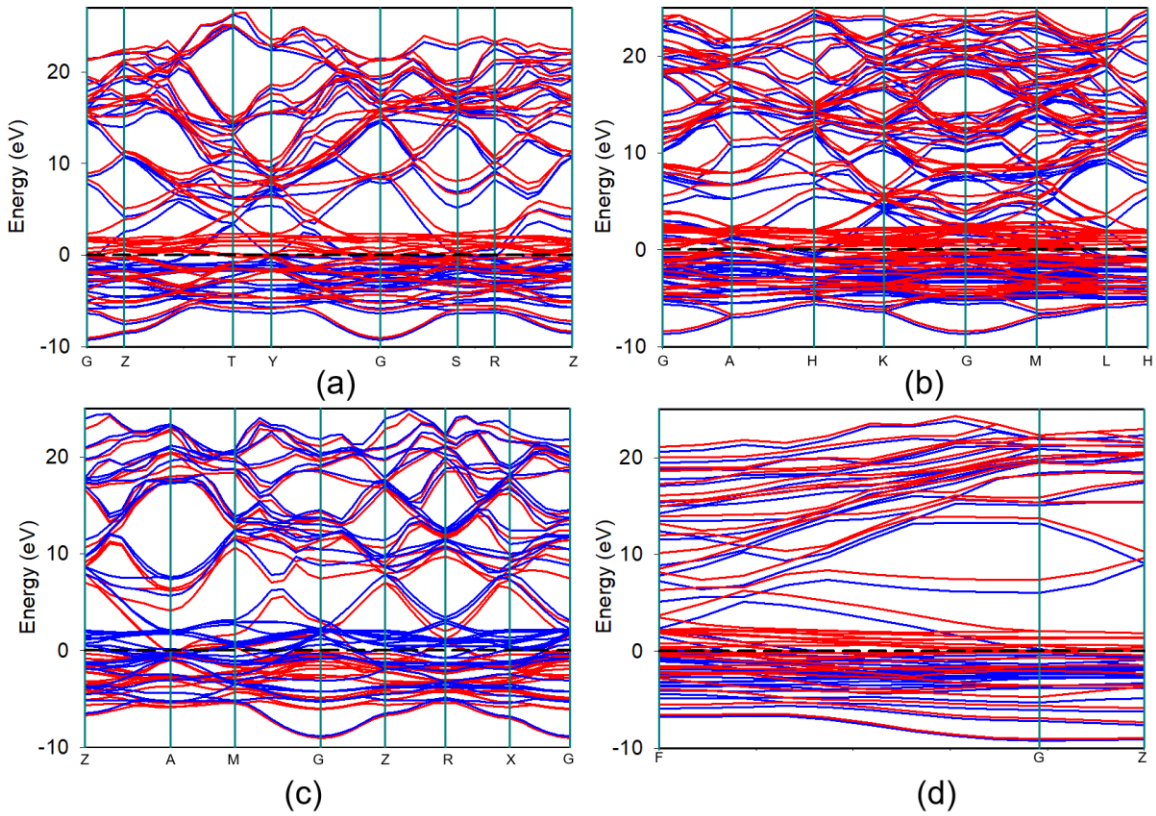

Figure 3. Electronic band structure plots of or $Cmmm$, $P63/mmc$, $P4/mmm$ and $R\bar{3}m$ of Fe_3Pt along high symmetry line in the Brillouin zone. The Fermi level is taken as the zero line ($E_F = 0eV$).

3.4. Mechanical Properties

Table 3 shows the calculated independent elastic constants (C_{ij}) and derived macroscopic properties of the orthorhombic, hexagonal, tetragonal and trigonal Fe_3Pt alloys at 0 K. CASTEP uses the generalized Hooke's law shown in equation 2) to fit the linear relationship between stress and strain components in the elastic regime to compute the independent elastic constants.

$$\sigma_i = \sum_j C_{ij}\varepsilon_j \tag{2}$$

where σ_i and ε_j are the Voigt notation components of the stress and strain tensor, respectively. Calculation and elastic constants and macroscopic mechanical properties are crucial in understanding the intrinsic mechanical stability, bonding nature and deformation behavior of solid-state materials. For any solid-state crystal lattice to be considered mechanically stable, certain stability conditions as postulated by Born must be satisfied [39].

Table 3. Calculated independent elastic constants and macroscopic properties of Fe_3Pt alloys.

Structure	C_{11}	C_{22}	C_{33}	C_{44}	C_{55}	C_{66}	C_{12}	C_{13}	C_{14}
$Cmmm$	300.43	298.95	224.53	120.12	119.83	36.27	92.71	161.85	
$P63/mmc$	249.31		22.23	-302.21			92.47	41.74	
$P4/mmm$	198.88		166.50	46.35		12.11	141.24	190.46	
$R\bar{3}m$	239.92		152.93	48.48			125.14	88.28	5.36
Macroscopic Properties (GPa)									
		B	G	E	σ	B/G		A	

 doi:10.20944/preprints202510.2084.v1

$Cmmm$	183.77	70.85	188.34	0.33	2.59	1.97
$P63/mmc$	57.87	-25.51	74.88	0.76	-2.27	-14.01
$P4/mmm$	179.09	38.75	108.44	0.40	4.62	-2.79
$R\bar{3}m$	131.99	52.15	138.23	0.33	2.53	0.24

Hexagonal crystals possess five independent elastic constants, while the tetragonal contain six due to the added $C_{66} = (C_{11} - C_{12})/2$. Since the Laue classes of the hexagonal and tetragonal crystal lattice have similar elastic matric, their Born necessary stability conditions are also similar and are given as [40]:

$$C_{11} > |C_{12}|;\ 2C_{13}^2 < C_{33}(C_{11} + C_{12});\ C_{44} > 0;\ C_{66} > 0 \tag{3}$$

The condition $C_{66} > 0$ is redundant for hexagonal crystal lattices. The trigonal or rhombohedral lattice has 6 independent elastic constants and like the hexagonal one $C_{66} = (C_{11} - C_{12})/2$ dependent. The following four conditions are sufficient for stability:

$$C_{11} > |C_{12}|;\ C_{44} > 0;\ C_{13}^2 < \frac{1}{2}C_{33}(C_{11} + C_{12});\ C_{14}^2 < \frac{1}{2}C_{44}(C_{11} - C_{12}) = C_{44}C_{66} \tag{4}$$

The orthorhombic crystal lattice with lower symmetry contains larger number (nine) independent elastic constants and the born stability conditions are:

$$C_{11} > 0;\ C_{11}C_{22} > C_{12}^2;\ C_{11}C_{22}C_{33} + 2C_{12}C_{13}C_{23} - C_{11}C_{23}^2 - C_{22}C_{13}^2 - C_{33}C_{12}^2 > 0; \tag{5}$$
$$C_{44} > 0;\ C_{55} > 0;\ C_{66} > 0$$

The independent elastic constants of the orthorhombic $Cmmm$, tetragonal $P4/mmm$ and trigonal $R\bar{3}m$ structures are positive and obey all the necessary Born stability conditions, which indicates mechanical stability. In contrast, the $P63/mmc$ phase exhibits anomalous elastic constants, due to a negative C_{44} value which violates the Born stability criteria. Such behavior signifies mechanical instability, suggesting that this hypothetical hexagonal structure cannot exist under ambient conditions and would spontaneously transform into a lower-symmetry, more stable phase with space group mmm [11, 41]. The elastic stiffness coefficients C_{11}, C_{22}, and C_{33} for the $Cmmm$-Fe_3Pt are relatively high, above 224.53 GPa, which signifies a strong resistance to axial deformation along all crystallographic directions. Furthermore, the off-diagonal $C_{12} = 92.71$ GPa and $C_{13} = 161.85$ GPa are also large, indicating considerable interplanar coupling, while the comparatively smaller shear constant (C_{66} =36.270 GPa) reveals moderate shear anisotropy. The $P4/mmm$-Fe_3Pt structure shows moderately high values of C_{11} and C_{33}, indicating fair axial stiffness. However, its small C_{66} value (12.11 GPa) reflects weak shear resistance, implying significant anisotropy in its mechanical response. The $R\bar{3}m$-Fe_3Pt phase displays intermediate stiffness with $C_{11} = 239.92$ GPa and $C_{33} = 152.93$ GPa, while the relatively small off-diagonal C_{14} value (5.36 GPa) indicates limited shear coupling.

The corresponding macroscopic mechanical properties representing a polycrystalline aggregate using Voigt–Reuss–Hill (VRH) averaging schemes were computed from the independent elastic constants to determined deformation characteristics [42]. Table 4 summarizes the expressions and descriptions of the calculated macroscopic properties.

Table 4. Mathematical expressions and descriptions of the macroscopic mechanical properties of the polycrystalline material. .

Property	Expression	Description
Bulk modulus (B)	$B_V = \frac{1}{9}(C_{11} + C_{22} + C_{33}) + \frac{2}{9}(C_{12} + C_{13} + C_{23})$ $B_R = [S_{11} + S_{22} + S_{33} + 2(S_{12} + S_{13} + S_{23})]^{-1}$ $B = \frac{B_V + B_R}{2}$	Resistance to uniform volume compression
Shear modulus (G)	$B_V = \frac{1}{15}(C_{11} + C_{22} + C_{33} - C_{12} - C_{13} - C_{23}) + \frac{1}{5}(C_{44} + C_{55} + C_{66})$ $B_R = 15[4(S_{11} + S_{22} + S_{33} - S_{12} - S_{13} - S_{23}) + 3(S_{44} + S_{55} + S_{66})]^{-1}$ $G = \frac{G_V + G_R}{2}$	Resistance to shape change

 doi:10.20944/preprints202510.2084.v1

Young's modulus (E)	$E = \frac{9BG}{3B + G}$	Stiffness
Poisson's ratio (σ)	$\sigma = \frac{3B - 2G}{6B + 2G}$	Ductility and brittleness
Pugh Ratio	$\frac{B}{G}$	Ductility
Anisotropy factor (A)	$A = \frac{2C_{44}}{C_{11} - C_{12}}$	Elastic anisotropy

S_{ij} represents the compliance tensor, the inverse of C_{ij}.

The $Cmmm$ Pphase shows large bulk modulus $B = 183.77$ GPa and shear modulus $G = 70.85$ GPa further confirming its robustness and greater resistance to compression, while the relatively high Young's modulus $E = 188.34$ GPa indicates good stiffness and metallic bonding characteristics. Moreover, the Pugh ($B/G = 2.59$) ratio greater than the critical value 1.5 of ductility and brittleness and Poisson's ratio ($\sigma = 0.33$) classifies this phase as ductile, while the positive anisotropy factor (A = 1.97) that diverge from unity suggests moderate elastic anisotropy.

The calculated Poisson's ratio ranges from 0.33 to 0.40, except for $P63/mmc$ are within the error limit (0.32 ± 0.09) and similar to $\sigma = 1/3$ recorded in most alloys [11, 43]. Consistent with the negative C_{44}, the hexagonal $P63/mmc$, shows a negative shear modulus and Pugh ration. Its Poisson ration is 0.76 which is beyond the metallic limit (~0.5), indicating that this phase exhibits extreme lateral expansion when compressed (or contraction when stretched), very high ductility, low shear resistance, and strong anisotropic bonding or magnetostrictive behavior. This phase likely reflects magnetoelastic softening, not purely mechanical elasticity. The bulk modulus (179.09 GPa) of the $P4/mmm$ phase is relatively larger than the shear (38.75 GPa), leading and larger Pugh ratio, confirming a ductile but less rigid nature relative to the orthorhombic phase. The moderate Poisson's ratio (0.40) also supports a metallic and ductile bonding character. Similar behavior is observed for the $R\bar{3}m$.

To further analyze the mechanical properties of the martensite Fe_3Pt alloys, we plotted stress vs strain profiles which represent the elastic response of crystal systems under applied strain, from which elastic constants and mechanical stability are evaluated. Figure 4 illustrates the calculated stress vs strain relationships for the $Cmmm$, $P63/mmc$, $P4/mmm$, and $R\bar{3}m$ phases of Fe_3Pt. The $Cmmm$, $P4/mmm$ and $R\bar{3}m$ structures exhibit smooth and well-defined linear elastic regions, 0% ≤ Strain ≤ 10% (red line) with strong correlations between the fitted and computed data ($R^2 = 0.980, 0.939$ and 0.970, respectively). This excellent agreement confirms excellent elastic behavior, numerical accuracy, mechanical stability with the elastic regime and validates the reliability of the derived elastic constants. Conversely, the hypothetical $P63/mmc$-Fe_3Pt phase displays a noticeable deviation from linearity even at small strains, reflected by a relatively low $R^2 = 0.860$. The irregular stress response suggests internal atomic relaxations or numerical instabilities during deformation, which consistent with the observed negative C_{44} elastic constant and shear modulus values. This behavior indicates that although predicted to be thermodynamically stable, the hypothetical $P63/mmc$–Fe_3Pt phase is mechanically unstable and prone to soft-mode distortions under elastic perturbation. Therefore, the combination of stress vs strain analysis and correlation fitting provides a robust means of assessing the elastic consistency and mechanical resilience of crystal systems.

 doi:10.20944/preprints202510.2084.v1

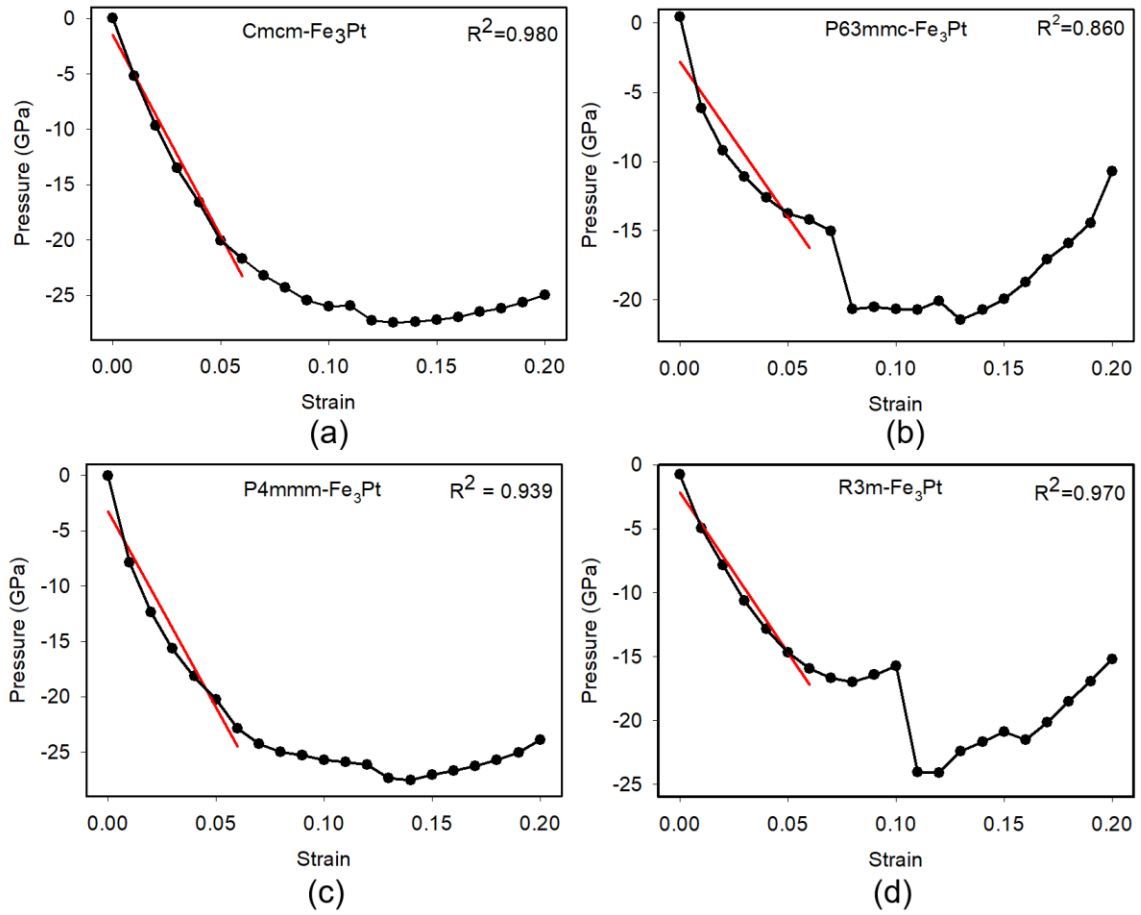

Figure 4. Stress vs strain curve with linear fit in the elastic region for Fe_3Pt alloys.

4. Conclusions

Density functional theory calculation on the martensite $Cmmm$, $P63/mmc$, $P4/mmm$ and $R\bar{3}m$ Fe_3Pt alloys were successfully carried out to determine the structural, thermodynamic, magnetic, electronic and mechanical properties. The negative enthalpies of formation showed that all the structures are thermodynamically stable. The substantial magnetic moments ranging from 2.94 μ_B to 3.04 μ_B and strong asymmetry of the spin up and down in the density of states plots, suggest strong magnetism and ferromagnetism behavior of the Fe_3Pt alloys. Calculations of independent and macroscopic elastic constant predicted mechanical stability on the $Cmmm$, $P4/mmm$ and $R\bar{3}m$ phases. However, the hypothetical $P63/mmc$ phase possesses negative C_{44} and shear modulus values, suggesting that it cannot exist under ambient conditions and would transform into a lower-symmetry and more stable phase. The observations collectively demonstrate that in addition to the $I4/mmm$-Fe_3Pt alloy, there exist other martensite $Cmmm$, $P4/mmm$ and $R\bar{3}m$ phases which are thermodynamically and mechanically stable, highly magnetic, strongly ferromagnetic, ductile, and stiff, consistent with their martensitic character.

References

1. R.L. Comstock, "Modern magnetic materials in data storage," J. Mater. Sci. Mater. Electron., vol. 13, p. 509, 2002.
2. M.R. Visokay and R. Sinclair, "Direct formation of ordered CoPt and FePt compound thin films by sputtering," Appl. Phys. Lett., vol. 66, p. 1692, 1995.

 doi:10.20944/preprints202510.2084.v1

3. M. Ohtake, S. Ouchi, F. Kirino and M. Futamoto, "L10 ordered phase formation in FePt, FePd, CoPt, and CoPd alloy thin films epitaxially grown on MgO(001) single-crystal substrates," J. Appl. Phys., vol. 111, p. 07A708, 2012.
4. R.A. Ristau, K. Barmak, L.H. Lewis, K.R. Coffey and J.K. Howard, "On the relationship of high coercivity and L10 ordered phase in CoPt and FePt thin films Available," J. Appl. Phys., vol. 86, p. 4527, 1999.
5. T.B. Massalski, Binary Alloy Phase Diagrams, Ohio: ASM International, 1990, p. 1752.
6. B. Wang; D. C. Berry; Y. Chiari; K. Barmak, "Experimental measurements of the heats of formation of Fe3Pt, FePt, and FePt3 using differential scanning calorimetry," J. Appl. Phys., vol. 110, p. 013903, 2011.
7. N.L. Lethole and P. Mukumba, "Ab Initio Studies of Mechanical, Dynamical, and Thermodynamic Properties of Fe-Pt Alloys," Materials, vol. 17, p. 3879, 2024.
8. M. Sternik, S. Couetm, J. Ła_zewski, P.T. Jochym, K. Parlinski and A. Vantomme, "Dynamical properties of ordered Fe-Pt alloys," J. Alloys Compd., vol. 651, p. 528, 2015.
9. Y. Kota and A. Sakuma, "Relationship between magnetocrystalline anisotropy and orbital magnetic moment in L10-type ordered and disordered alloys," J. Phys. Soc. Jpn., vol. 81, p. 84705, 2012.
10. J. Lyubina, I. Opahle, M. Richter, O. Gutfleisch, K.H. Müller, L. Schultz and O. Isnard, "Influence of composition and order on the magnetism of Fe–Pt alloys: Neutron powder diffraction and theory," Appl. Phys. Lett., vol. 89, p. 032506, 2006.
11. N. Zotov and A. Ludwig, "First-principles calculations of the elastic constants of FeePt alloys," Intermetallics, vol. 16, p. 113, 2008.
12. N. Lethole, P. Ngoepe and H. Chauke, "Compositional Dependence of Magnetocrystalline Anisotropy, Magnetic Moments, and Energetic and Electronic Properties on Fe-Pt Alloys," Materials, vol. 15, p. 5679, 2022.
13. T. Shima, K. Takanashi, Y.K. Takahashi and K. Hono, "Coercivity exceeding 100 kOe in epitaxially grown FePt sputtered films," Appl. Phys. Lett. , vol. 85, p. 2571, 2004.
14. S. Muto, R. Oshima and F.-E. Fujita, "Nucleation and growth in martensitic transformations of ordered Fe3Pt alloys," Metall.Trans., vol. 19, p. 2931, 1988.
15. M. Yamamoto, T. Fukuda, T. Kakeshita and K. Takahashi, "Orthorhombic martensiteformedinL12-type Fe3Pt Invaralloy," J. Alloys Compd., vol. 577S, p. S503, 2013.
16. Y. Nakata, "The Crystal Structure and Magnetic Properties of Fe3Pt Martensite Determined by First Principle Calculations," Mater. Trans., vol. 44, p. 1706, 2003.
17. T. Fukuda and T. Kakeshita, "Lattice Softening in Fe3Pt Exhibiting Three Types of Martensitic Transformations," Metals, vol. 7, p. 156, 2017.
18. T. Tadaki, Y. Nakata and K. Shimizu, "Anomalous reflections in low temperature electron diffraction from the thermoelastic martensite in a fully ordered Fe-Pt Alloy," Mater. Sci. Forum, vol. 169, p. 56, 1990.
19. T. Tadaki, Y. Nakata and K. Shirnizu, "Occupancy Sites of Constituent Atoms and their Effects on the Martensitic Transformations in some Cu-Based and Ti-Ni-Based Ternary Alloys," J. Phys. IV, vol. 5, pp. C8-81, 1995.
20. M.K. Horton et al., "Accelerated data-driven materials science with the Materials Project," Nat. Mater, vol. 24, p. 1522, 2025.
21. A. Jain, S.P. Ong, G. Hautier, W. Chen, W.D. Richards, S. Dacek, S. Cholia; D. Gunter, D. Skinner, G. Ceder and K.A. Persson, "Commentary: The Materials Project: A materials genome approach to accelerating materials innovation," APL Mater., vol. 1, p. 011002, 2013.
22. Z.H. Liu, Y.J. Zhang, G.D. Liu, B. Ding, E.K. Liu, H.M. Jafri, Z.P. Hou, W.H. Wang, X.Q. Ma and G.H. Wu, "Transition from Anomalous Hall Effect to Topological Hall Effect in Hexagonal Non-Collinear Magnet Mn3Ga," Sci. Rep., vol. 7, p. 515, 2017.
23. K. Zellagui, M. Khedidji and H. Yousfi, "First-principles study of the structural, electronic, dielectric, and dynamical properties of gallium nitride in the graphite-like hexagonal P63/mmc phase," Theor. Chem. Acc., vol. 143, p. 79, 2024.
24. B.O. Mnisi, E.M. Benecha and M.M. Tibane, "Density functional theory study of phase stability and electronic properties for L12 X3Ru and XRu3 alloys," Eur. Phys. J. B, vol. 98, p. 106, 2025.

 doi:10.20944/preprints202510.2084.v1

25. B. Thacker, T. Akhani, M.B. Solanki and R.N. Kharatmol, "Theoretical investigation in structural, electronic, vibrational, thermophysical, thermoelectric, and elastic properties of L12 and L12 FePd3 alloys by a DFT approach," Theor. Chem. Acc., vol. 144, p. 78, 2025.
26. B. Thacker, M.B. Solanki, R. Kharatmol, Y.D. Kale and T. Akhani, "Exploring Structural, Electronic, Vibrational, and Thermophysical Properties of Fe–Pt, Fe3–Pt, and Fe–Pt3 Alloys: A Density Functional Theory Study," Phys. Status Solidi B, vol. 262, p. 2400160, 2024.
27. S.J. Clark, M.D. Segall, C.J. Pickard, P.J. Hasnip, M.I.J. Probert, K. Refson and M.C. Payne, "First principles methods using CASTEP," Z. Kristallogr., vol. 220, p. 567, 2005.
28. J.P. Perdew, K. Burke and M. Ernzerhof, "Generalized Gradient Approximation Made Simple," Phys. Rev. Lett., vol. 77, p. 3865, 1996.
29. P. Hohenberg and W. Kohn, "Inhomogeneous electron gas," Phys. Rev., vol. 136, p. B964, 1964.
30. H.J. Monkhorst and J.D. Pack, "Special points for Brillouin-zone integrations," Phys. Rev. B, vol. 16, p. 1748, 1977.
31. J. Aarons, "A New CASTEP and ONETEP Geometry Optimiser," http://www.hector.ac.uk/cse/distributedcse/reports/castep-geom/castep-geom/HTML/dCSE_project.html.
32. B.G. Pfrommer, M. Cote, S.G. Louie and M.L. Cohen, "Relaxation of Crystals with the Quasi-Newton Method," J. Comput. Phys., vol. 131, p. 233, 1997.
33. D. Packwood, J. Kermode, L. Mones, N. Bernstein, J. Woolley, N. Gould, C. Ortner and G. Csányi, "A universal preconditioner for simulating condensed phase materials," J. Chem. Phys. , vol. 144, p. 164109, 2016.
34. K.H.J. Buschow, P.G. van Engen and R. Jongebreur, "Magneto-optical properties of metallic ferromagnetic materials," J. Magn. Magn. Mater., vol. 38, p. 1, 1983.
35. J.M. MacLaren, R.R. Duplessis, R.A. Stern and S. Willoughby, "First Principles Calculations of FePt, CoPt, Co3Pt, and Fe3Pt Alloys," IEEE Trans. Magn., vol. 41, p. 4374, 2005.
36. T. Cheng, G. Yu, Y. Su, C. Ge, X. Zhang, L. Zhu and L. Li, "Lattice dynamics, elasticity and magnetic abnormality in ordered crystalline alloys Fe3Pt at high pressures," J. Magn. Magn. Mater., vol. 453, p. 67, 2018.
37. M. Li, H. Pi, Y. Zhao, T. Lin, Q. Zhang, X. Hu, C. Xiong, Z. Qiu, L. Wang, Y. Zhang, J. Cai, W. Liu, J. Sun, F. Hu, L. Gu, H. Weng, Q. Wu, S. Wang, Y. Chen and B. Shen, "Large Anomalous Nernst Effects at Room Temperature in Fe3Pt Thin Films," Adv. Mater., vol. 35, p. 2301339, 2023.
38. K. Aledealat, B. Aladerah, A. Obeidat and M. Gharaibeh, "First-principles study of electronic structure and magnetic properties of L10-ordered FeNi, FePd, and FePt alloys," Heliyon, vol. 7, p. e08639, 2021.
39. M. Born and K. Huang, "Dynamics Theory of Crystal Lattices," Oxford University Press, 1954.
40. F. Mouhat and F.X. Coudert, "Necessary and Sufficient Elastic Stability Conditions in Various Crystal Systems," Phys. Rev. B, vol. 90, p. 224104, 2014.
41. T. Paszkiewicz, M. Pruchnik and P. Zieliński , "Unified description of elastic and acoustic properties of cubic media: elastic instabilities, phase transitions and soft modes," Eur. Phys. J. B, vol. 24, p. 327, 2001.
42. R. Hill, "The Elastic Behaviour of a Crystalline Aggregate," Proc. Phys. Soc., vol. A65, p. 349, 1952.
43. A. Al-Ghaferi, P. Mullner, H. Heinrich, G. Kostorz and J.M.K. Wiezorek , "Elastic Constants of Equiatomic L10Ordered FePd Single Crystals," Acta Materialia, vol. 54, p. 881, 2006.